Laser Engineered Multilayer Coating of Biphasic Calcium Phosphate/Titanium Nanocomposite on Metal Substrates

Martin Yi Zhang,[†] Chang Ye,[†] Uriel Joseph Erasquin,[‡] Toan Huynh,[‡] Chengzhi Cai,[‡] and Gary J. Cheng*,[†]

[†]School of Industrial Engineering, Purdue University, West Lafayette, Indiana 47906

[‡]Department of Chemistry, University of Houston, Houston, Texas 77204

S *Supporting Information*

ABSTRACT: In this work, laser coating of biphasic calcium phosphate/titanium (BCP/Ti) nanocomposite on Ti-6Al-4 V substrates was developed. A continuous wave neodymium-doped yttrium aluminium garnet (Nd:YAG) laser was used to form a robust multilayer of BCP/Ti nanocomposite starting from hydroxyapatite and titanium nanoparticles. In this process, low power coating is realized because of the strong laser—nanoparticle interaction and good sinterability of nanosized titanium. To guide the optimization of laser processing conditions for the coating process, a multiphysics model coupling electromagnetic module with heat transfer module was developed. This model was validated by laser coating experiments. Important features of the coated samples, including microstructures, chemical compositions, and interfacial bonding strength, were characterized. We found that a multilayer of BCP, consisting of 72% hydroxyapatite (HA) and 28% beta-tricalcium phosphate (β-TCP), and titanium nanocomposite was formed on Ti-6Al-4 V substrates. Significantly, the coating/substrate interfacial bonding strength was found to be two times higher than that of the commercial plasma sprayed coatings. Preliminary cell culture studies showed that the resultant BCP/Ti nanocomposite coating supported the adhesion and proliferation of osteoblast-like UMR-106 cells.

KEYWORDS: laser coating, nanoparticles, BCP/Ti nanocomposite, functional gradient coating, interfacial bonding strength, biocompatibility
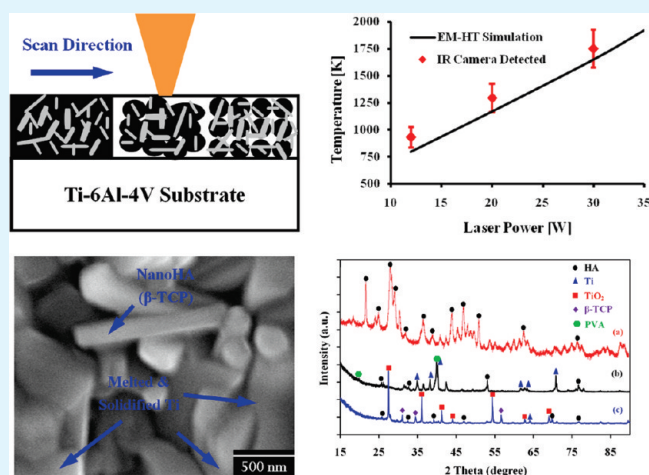
1. INTRODUCTION

Biphasic calcium phosphate (BCP) is a bioceramic that has similar chemical composition to natural human bones and teeth. It consists of a mixture of hydroxyapatite (HA, $Ca_{10}(PO_4)_6(OH)_2$), and beta-tricalcium phosphate (β-TCP, $Ca_3(PO_4)_2$). BCP possesses the combined properties of both stable (HA) and unstable (β-TCP) phases. Although HA implants are highly stable, β-TCP can be readily dissolved in physiological environment. BCP mixtures have been widely used in artificial bone and tooth implants;[1] delivery of drugs, antibiotics and hormones;[2] and nasal septum repair.[3]

BCP are commonly prepared by sintering commercially available tricalcium phosphate (TCP) or precipitated apatites.[4] BCP with varying HA and β-TCP components are usually formed by sintering calcium deficient apatites of varying Ca/P molar ratio.[5] However, because of their natural brittleness, HA and β-TCP has unfavorable hardness, ductility, and toughness,[6] which greatly reduces the lifetime of load bearing implants. To achieve good durability of the BCP ceramics implants, the mechanical strength, fixation ability, and osteoconductive properties of the materials must be improved. BCP ceramics are commonly coated on metal substrates using a variety of methods, including plasma spraying,[5,7] precipitation,[8] dip coating,[9,10] electrochemical deposition,[11] salt leaching,[12] pulsed electrodeposition,[13] and flame spray pyrolysis.[14] However, these coating techniques have at least one of the following drawbacks: (i) weak coating/substrate interfacial bonding strength,[15] (ii) non-uniformity of coating,[16] (iii) mismatch of thermal and mechanical properties due to sharp interface,[17] and (iv) limited thickness.

In this work, we have developed a new method for low laser power coating of BCP/Ti nanocomposite on Ti-6Al-4 V substrates based on localized laser heating. This method addresses the above drawbacks. In addition, the composition of HA and β-TCP in the BCP coating can be varied by controlling the laser
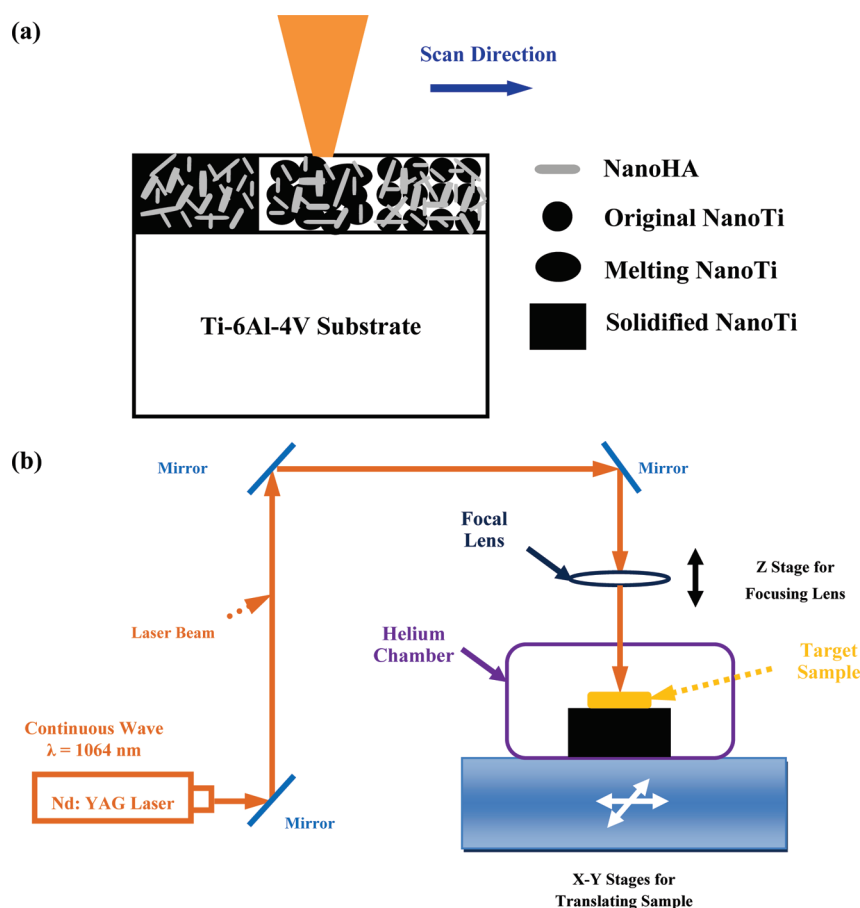
Figure 1. (a) Experimental schematic of laser coating of BCP/Ti nanocomposite on metal substrates and (b) experimental layout.

power. Specifically, a mixture of HA nanoparticles (nanoHA) and Ti nanoparticles (nanoTi) is first coated on the substrate. The coating is then exposed to laser irradiation that converts the nanoHA and nanoTi mixture (nanoHA/Ti) layer into a robust BCP/Ti nanocomposite coating. Since conversion of nanoHA into β-TCP occurs above a threshold temperature, by varying the laser power, the amount of β-TCP formed in the composite could be controlled.

Another novelty of this approach is the employment of titanium nanoparticles. Depending on the size, nanoTi possesses a higher laser adsorption cross-section and plasmon resonance.[18,19] Therefore, upon lower laser irradiation, the nanoTi can be melted to form a liquid network entrapping the nanoHA in the composite. The liquid Ti network also maximizes the contact with the substrate. After solidification, this process results in a tight integration of the coating with the substrate, as illustrated by Figure 1a. Note that nanoHA is almost transparent to the 1064 nm infrared laser[20] used in this study, whereas the laser energy is almost exclusively adsorbed by the nanoTi followed by heat transfer to the surrounding nanoHA.

A gradient coating scheme can also be realized by this method to further enhance the coating properties. In this scheme, the nanoHA/Ti ratio in the pre-coated composite layers is decreased from the coating/substrate interface towards the top surface. The high content of Ti at the substrate interface greatly reduces coating substrate mismatch, resulting in a high degree of integration with the substrate and enhanced coating/substrate interfacial strength. To demonstrate this approach, we first deposited

layer-by-layer of nanoHA/Ti with increasing ratio on a Ti-6Al-4 V substrate by dip-coating of polyvinyl alcohol (PVA) solutions of the mixtures of nanoHA and nanoTi. Laser beam was then applied to heat the pre-coated substrate. Controlling the temperature is critical because nanoTi needs to be melted and nanoHA to be partially decomposed.

To find optimal processing conditions, we built a multiphysics model by coupling electromagnetic module with heat transfer module. This model is used to propose a mechanism for the laser coating process, and is validated experimentally. After laser coating, several important features of the nanoHA/Ti coatings are characterized, including the microstructures, chemical compositions, surface roughness and porosity, and interfacial bonding strength between coating and substrate. Furthermore, preliminary cell culture experiment on the nanoHA/Ti coatings is performed to demonstrate that the coating supports the adhesion and proliferation of osteoblast cells.

2. MATERIALS AND METHODS

2.1. Formation of NanoHA. Two types of nanoHA were used in current investigation: fiber and spherical shapes. The fiber-shaped nanoHA was purchased from Shanghai Rebone Biomaterials Co., Ltd, with nominal diameter ranging from 20-50 nm, and length ranging from 400-800 nm. Spherical nanoHA was prepared similarly to the literature method.[21] A 0.6 M solution of $(NH_4)_2HPO_4$ and a 1.0 M solution of $Ca(NO_3)_2$ was prepared. The pH of the latter solution was adjusted to 10 using concentrated NH_4OH. HA was formed by the drop-wise
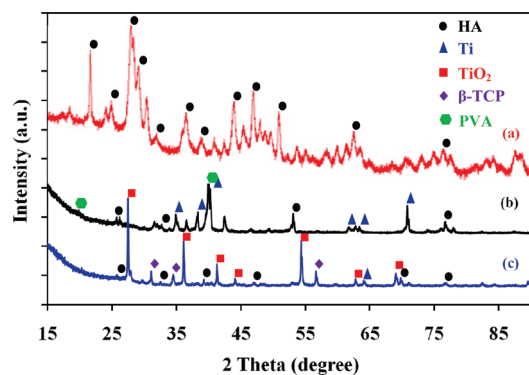
Figure 2. X-ray diffraction patterns of (a) original nanoHA powder, (b) dip-coated pre-coating layer, (c) laser coated double-layer BCP/Ti nanocomposite. The obtained XRD peaks were compared to HA (PDF Ref. 74-0566), β-TCP (PDF Ref. 09-0169), Ti (PDF Ref. 44-1294), and TiO$_2$ (PDF Ref. 21-1276). The doublet peaks of PVA were observed in dip-coated sample b, but not in the laser-coated sample c. Cu K$_\alpha$ radiation was used (λ = 1.54178 Å).

addition of the Ca(NO$_3$)$_2$ solution with stirring to the (NH$_4$)$_2$HPO$_4$ solution at a rate of 6−7 drops every 5 s. The formation of HA could be described by the following formula:

$$10Ca(NO_3)_2 + 6(NH_4)_2HPO_4 + 8NH_4OH$$
$$\rightarrow Ca_{10}(PO_4)_6(OH)_2 + H_2O + 20NH_4NO_3$$
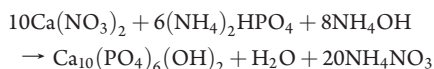
The solution was then left to stand and equilibrate for 20 h at room temperature with continuous stirring. The resulting white precipitate was washed 3 times with Milli-Q water and centrifuged at 2500 rpm for 2 minutes to separate the HA. The wet white powdery residue was pooled together and heated in a temperature-controlled furnace at 200°C for 20 h. After cooling, the product formed a coalesced mass of white opaque solid which was then grounded with a pestle and mortar. The powder was characterized by X-ray diffraction (XRD) using Bruker AXS D8 focus X-ray powder diffractometer as shown Figure 2a. The X-ray source generator was set at 40 KV and 40 mA, with the 2θ angle starting from 20° and ending at 90° with a stepping of 0.01°. The powder was confirmed to be mainly HA by comparing the XRD pattern with Powder Diffraction File (PDF) Ref. 74-0566 (HA, synthesis). No peaks for other phases were found.

2.2. Dispersion of NanoHA/Ti. NanoTi were purchased from Nanostructured & Amorphous Materials, Inc. Water-soluble polyvinyl-alcohol (PVA, Sigma-Aldrich, USA), which has good layer forming, emulsifying and adhesive properties, was used to disperse the nanoparticles. PVA powder was added slowly into hot distilled water to form a 4% (wt %) solution in a clean beaker. The beaker was covered by aluminum foil and the solution was stirred for about 4 h using a magnetic stirrer until it became clear. Then the PVA solution was cooled down to room temperature. HA and Ti nanoparticles were then added into the PVA solution and stirred until the nanoHA and nanoTi were evenly distributed in the solution. Two types of nanoHA/Ti mixture with different mixing ratio (wt %) were prepared: 50%HA/50%Ti and 80%HA/20%Ti.

2.3. Dip Coating. Dip coater with a thermal-controlled chamber (with temperature set at 363 K) was used to perform nanoHA/Ti pre-coating on flat Ti-6Al-4 V substrates. The Ti-6Al-4 V substrate was first prepared by sand-paper polishing, followed by oxygen plasma treatment for 60s to increase the substrate hydrophilicity. The thickness of the coating was controlled by withdrawal speed and the viscosity of the solution. Multilayer of nanoHA/Ti coatings can be formed by repeating the dip-coating process with coating solution of varied nanoHA/Ti mixing ratio. A representative dip-coated nanoHA/Ti sample was characterized

by XRD as shown in Figure 2b. Peaks of HA (Ref. 74-0566) and Ti (Ref. 44-1294) were indexed and found as expected.

2.4. Laser Coating. Neodymium-doped yttrium aluminium garnet (Nd:YAG) laser operating in continuous wave (CW) mode with wavelength of 1064 nm was employed. The experimental layout is illustrated in Figure 1b. After three reflection mirrors, laser beam was focused to obtain the desired beam radius. The dip-coated sample was placed in a closed chamber purged with Helium. The sample moving relative to laser beam was controlled by a motorized x−y stage.

Different laser processing conditions were tested for coating nano-HA/Ti on Ti-6Al-4 V substrate in order to achieve the following three properties: (i) favorable chemical composition of BCP/Ti nanocomposite (gradient composition with mixing ratio of 80%HA:20%Ti in the outer layer and 50%HA:50%Ti in the inner layer), (ii) strong coating/substrate interfacial bonding, and (iii) beneficial biocompatibility. Systematic optimizations were carried out in finding the optimal processing parameters to achieve these properties in laser engineered low power coating of nanoBCP/Ti nanocomposite. The processing parameters include laser power (12 to 30 W), laser scanning speed (0.5 to 2 mm/s), and laser beam radius (0.3 to 1 mm) for coatings with different thickness (20 and 40 μm). Details will be discussed in section 3.1.

2.5. Characterizations. Surface and cross-section morphological study was performed by field emission scanning electron microscopy (FESEM) using Hitachi S-4800. The accelerating voltage used was 5 kV. The magnifications used ranged from several thousands to several hundreds of thousands times. In order to determine the chemical composition before and after laser coating, selected area energy dispersive X-ray spectrometry (SAEDS) and elemental mapping were employed to characterize the chemical composition of the coatings with a high spatial resolution. JSM 6400 scanning electron microscope system equipped with energy dispersive X-ray spectrometry (EDS) detector was employed to perform SAEDS and elemental mapping. Before spectrum analyzing, a calibration process was conducted against pure copper tape. The calibration file is then saved for reference. After properly calibration, spectra of the region of interests (ROIs) were obtained. The integrated counts in the elements region of interests were obtained for relative probability of calcium and phosphorus. Elemental mapping showing the spatial distribution of elements (Ca, P, and Ti) in our sample was produced by scanning the electron beam over a ROI area of 60 x 80 μm^2. XRD was performed to determine the crystallographic structure and phase of calcium phosphate, using a Bruker AXS D8 focus X-ray diffractometer. The X-ray source generator was set at 40 KV and 40 mA, with the 2θ angle starting at 20° and ending at 90° with a stepping of 0.01°.

2.6. Multiphysics EM-HT Simulation. The laser processing parameters consist of laser wavelength, laser intensity (determined by laser power and laser beam size), and laser scanning speed. We used a 1064 nm laser because HA absorbs very little in the infrared region,[17,22] whereas nanoTi and titanium alloy substrates take most of the laser incident energy. The mechanism of laser coating of BCP/Ti nanocomposites on metal substrate is not fully understood. The interaction between laser and nanoTi is complicated since the wavelength of laser is much greater than the nanomaterials and the coatings cannot be assumed as continuous materials. To understand the laser coating mechanism, and select appropriate laser processing conditions, multiphysics simulation of laser interaction with nanoHA/Ti is performed using ComSol. There are two sub-modules in the model: electromagnetic (EM) module and coupled heat transfer (HT) module. The schematic of multiphysics EM-HT simulation modeling is shown in Figure S1 in the Supporting Information and corresponding 2D finite element model (FEM) model is established as shown in Figure S2 in the Supporting Information.

The precoated layer is composed of closely packed nanoHA and nanoTi particles; as a result, near-field scattering happens because of nanoparticles, and enhances the local optical intensity close to the surface of nanoparticles. The absorbed energy releases in the form of resistive heating.

The EM module is established to investigate the resistive heating as a result of laser-nanoparticle interaction, and examine how resistive heating was formed and hence heated up nanoparticles. Ampère's law with Maxwell's correction and Faraday's law of induction are the governing equations of the EM module. Combining the Poynting's theorem,[23] the following equation (eq 1) could be obtained:

$$\int_V JEdV + \oint_S (EH)nds = -\int_V \left(E\frac{\partial D}{\partial t} + H\frac{\partial B}{\partial t}\right)dV \qquad (1)$$

where: the first term on the left represents the resistive losses, and the second term denotes the radiative losses. According to ComSol v3.3 user's guide, the resistive heating (Q_{HT}: W/m^3) can be expressed as the following (eq 2):

$$Q_{HTT} = \frac{1}{2} Re\{\sigma EE^* - j\omega ED^*\} \qquad (2)$$

With the resistive heating calculated from by EM module, it is then input into the HT module as the heat source. The coupled HT module is used to compute the resulting temperature as a result of resistive heating induced by laser-nanoparticle interactions. The heat transfer process can be modeled by heat diffusion mechanism[24] for a continuous wave laser irradiation where the laser duration (in the order of nanoseconds) is much longer than the electron-photon relaxation time (in the order of tens of picoseconds). The governing equation for heat diffusion can be expressed as follows (eq 3):

$$\rho C_p \frac{\partial T}{\partial t} + \nabla(-\kappa \nabla T) = Q \qquad (3)$$

where $Q = Q_{HT}$ is the resistive heating calculated from (eq 2).

Other than heat source, thermal properties (e.g. thermal conductivity, heat capacity, and density) were also applied to define involved materials. The final output of the EM-HT model was temperature distribution. A typical distribution of resistive heating and resulting temperature distribution is shown Figures S3 and S4 in the Supporting Information. Figure S3 in the Supporting Information shows that resistive heating typically occurred only in nanoTi, since only nanoTi is interact with laser with 1064 nm wavelength. Figure S4 in the Supporting Information shows that temperature elevation occurs in both HA and Ti particles as a result of heat energy transfer. More details on the modeling of multiphysics simulation can be found in Supporting Information and our previous report.[22]

3. RESULTS

3.1. Effects of Laser Power on Temperature.
Multiphysics simulation indicates that the temperature on nanoHA/Ti coating is strongly dependent on laser intensity applied. A representative example of the calculated temperature field (Figure 3a) and history profile (Figure 3b) along the 40 μm thick (double-layer) nanoHA/Ti (50%HA/50%Ti in the inner layer, and 80%HA/20%Ti in the outer layer) coating on a Ti-6Al-4 V substrate. The laser processing parameters used are: laser power 30 W, laser beam radius 0.5 mm, and scanning speed 1 mm/s. The shape and size distribution of the nanoHA (rectangles and ellipses) and nanoTi (circles) used for the simulation are based on the field emission scanning electron microscopy (FESEM) image (Figure 3c) of a film of composite of nanoHA/Ti (80%HA/20%Ti in the outer layer). Figure 3a shows that under this condition, the temperature was about 1105 K near the surface of the coating, and increased to 1911 K at the coating/substrate interface. The temperature history in the first 3 milliseconds (ms) after laser irradiation was plotted in Figure 3b. At the beginning, temperature in both layers started to increase. The temperature of interfacial layer reached the peak at 0.8 ms, whereas nanoHA layer reaches peak at 1.2 ms. After the

peaks, both temperature continuously dropped to ~1000 K within 3 ms.

Accordingly, experiments were carried out to validate the simulation results, as summarized in Figure 4. The laser processing conditions were: CW laser beam with power of 12 to 30 W, laser scanning speed of 1 mm/s and laser beam radius of 0.5 mm. As shown in Figure 4a, the temperature increases with increasing of laser power. There is a good agreement found in resulting temperature between simulation and experiments. Both simulation and experimental data show that the surface temperature increases almost linearly with applied laser power. A representative IR camera temperature frame was presented in Figure 4b obtained with $P = 18$ W for a 40 μm thick nanoHA/Ti (double-layer) coating on a Ti-6Al-4 V substrate. The maximum temperature detected was 1163±100 K. After series of trails-and-errors and systematic optimizations, the optimal conditions found for the single-layer nanoHA/Ti (50%HA/50%Ti) sample was 18 W, whereas it was 30 W for the double-layer nanoHA/Ti (50%HA/50%Ti in the inner layer, and 80%HA/20%Ti in the outer layer) sample. The optimal laser scanning speed was 1 mm/s and laser beam radius was 0.5 mm.

3.2. Surface Microstructure Analysis.
FESEM characterizations were carried out to investigate the surface morphological changes of nanoTi during the laser coating process. Images a and b Figure 5show the dip-coated nanoHA/Ti on substrate before laser processing. The samples were double-layered coatings with 50%HA/50%Ti in the inner layer, and 80%HA/20%Ti in the outer layer. Two types of nanoHA were used: left images show the fiber-shaped nanoHA mixed with nanoTi, and right images show the spherical nanoHA mixed with nanoTi. PVA polymer was used as the confinement media to bond nanoHA/Ti layer on the metal substrate. After laser coating, as shown in Figure 5c and d, the morphology of fiber-shape and spherical nanoHA remained the same, while most of the titanium nanospheres were melted and merged together to encapsulate the nanoHA. The molten and resolidified nanoTi formed a strong metallurgical bonding between Ti-6Al-4 V substrate and the laser-processed coating.

3.3. Compositional and Structural Analysis.
Morphology studies can only tell the change in physical appearance of involved nanoparticles, but compositional and structural analysis could determine how those nanoparticles are chemically altered. In this study, selected area energy-dispersive X-ray spectrometry (SAEDS) and elemental mapping was employed to characterize the chemical composition of the coatings with a high spatial resolution. The integrated counts of the element region of interests (ROIs) were obtained for relative probability of calcium and phosphorus. Spectra of selected area of the double layer sample are shown in Figures 6a−c. Figure 6a showed a typical HA nanoparticle where no decomposition occurred after laser processing with power of 30 W. The Ca/P ratio was 1.66, which is very close to the stoichiometric of Ca/P in original HA (1.67). However, a larger area scanning of the same sample gave a spectrum, as shown in Figure 6b, where the molar ratio of Ca/P was found to be 1.62±0.1. These statistical data (standard deviation) were obtained by selecting 3 different areas on 3 separate double-layer samples after a 25 min data collection for each spectrum. The decline in Ca/P ratio is likely due to the decomposition of HA into β-TCP.[2] In agreement, it was reported that partial conversion of HA to β-TCP occurred at <1125 °C,[25] resulting in formation of a mixture of HA and β-TCP, i.e., the biphasic calcium phosphate (BCP).

Figure 6d−f showed the elemental mapping of calcium, phosphate, and titanium over a 60 x 80 μm^2 rectangular area. The
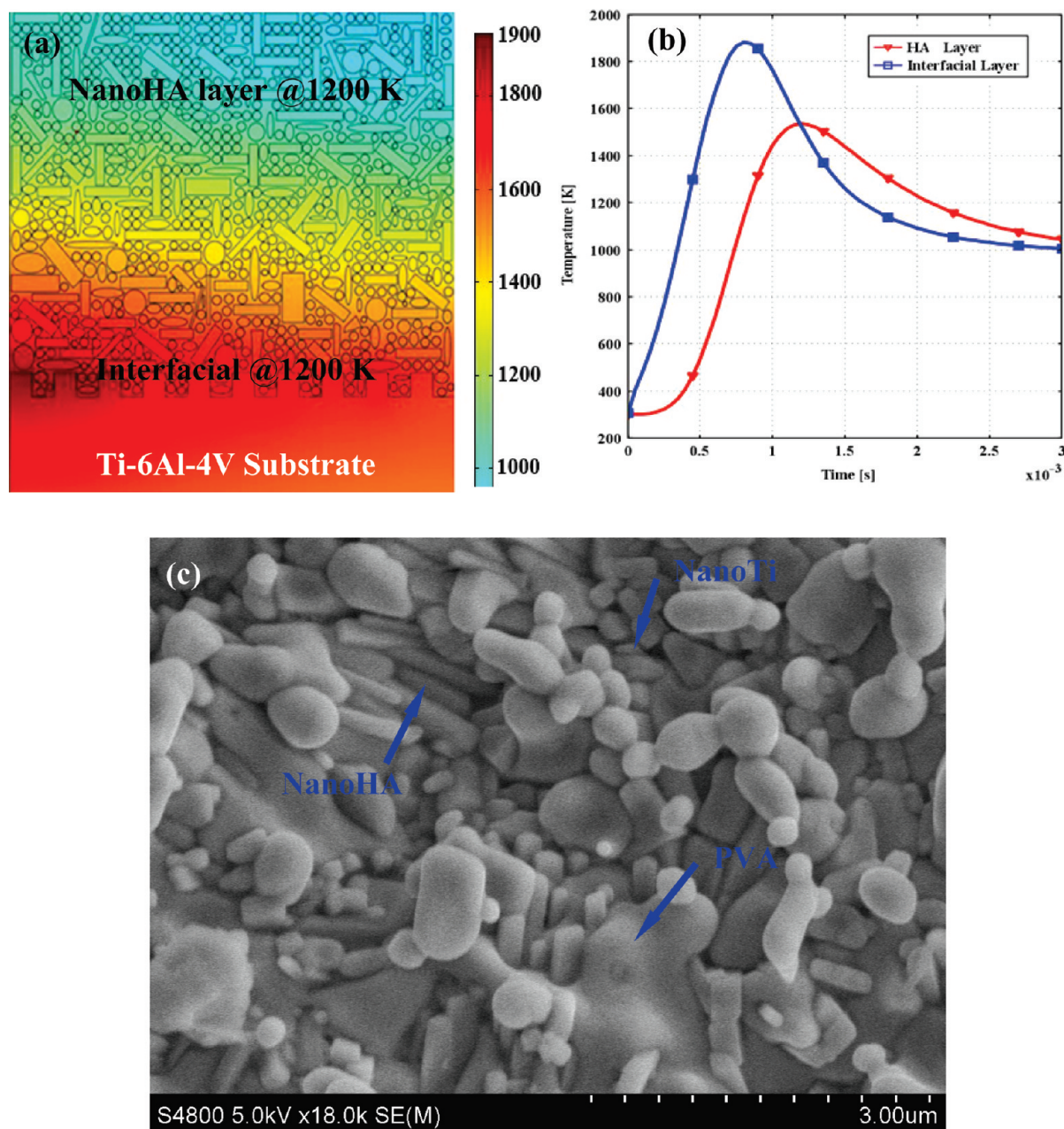
Figure 3. Typical simulated temperature field (a) and history profile (b) of BCP/Ti nanocomposite on Ti-6Al-4 V upon laser treatment, computed by the EM-HT coupled model at ComSol platform, using the following parameters: double-layer sample with thickness of 40 μm, laser power 30 W, laser beam radius 0.5 mm, and scanning speed 1 mm/s. (b) A typical FESEM image of pre-coated nanoHA/Ti mixture on which simulation modeling wais based.

results suggested that: (i) Ca and P were located in the exact same region. (ii) Ti was complementary to Ca and P. However, this does not indicate phase separation between BCP and titanium because the region scanned was a few orders of magnitude larger than the nanoparticle size. The elemental mapping does indicate that the distribution of nanoHA and nanoTi is not perfectly even, aggregation of each of these two types of nanoparticles occurred during laser coating. (iii) BCP had a higher concentration than nanoTi in the top layer of the selected region. This result is expected because the top layer starting material of the sample was 80% HA/20%Ti.

The formation of β-TCP was also confirmed by XRD. As shown in Figure 2c, peaks of HA (Ref. 74-0566), β-TCP (Ref. 09-0169),

and TiO$_2$ (Ref. 21-1276) were found in the XRD pattern after laser coating. However, no β-TCP was found in neither nanoHA powder (a) nor pre-coating (b), which suggested that β-TCP was introduced by laser irradiation. TiO$_2$ peaks were found because oxidization occurred during laser coating likely by trace amounts of oxygen present in the Helium atmosphere.

The SAEDS spectrum of a typical nanoTi was given in Figure 6c. It shows that the major signals are titanium, with minor signals (V) coming from the substrate. PVA was reported to have a boiling point of 500 K.[26] When laser irradiation produced a peak temperature of about 1100 K, PVA was vaporized from the BCP/Ti nanocomposite coating. Indeed, no PVA peak was found in the XRD spectrum after laser coating (Figure 2c).
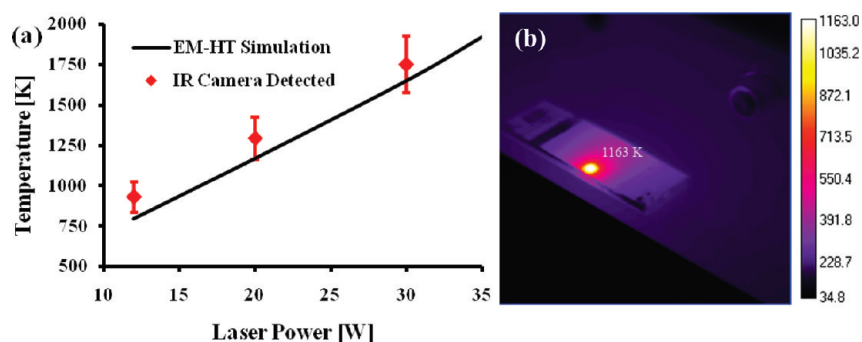
Figure 4. (a) Plot of simulated and measured temperature of a 40 μm thick nanoHA/Ti (50%HA/50%Ti in the inner layer, and 80%HA/20%Ti in the outer layer) coating on a Ti-6Al-4 V substrate as a function of laser power; and (b) a real-time image captured by calibrated infrared camera during laser irradiation with a power of 18 W, using a 1064 nm laser with a beam radius of 0.5 mm and scan speed of 1 mm/s.
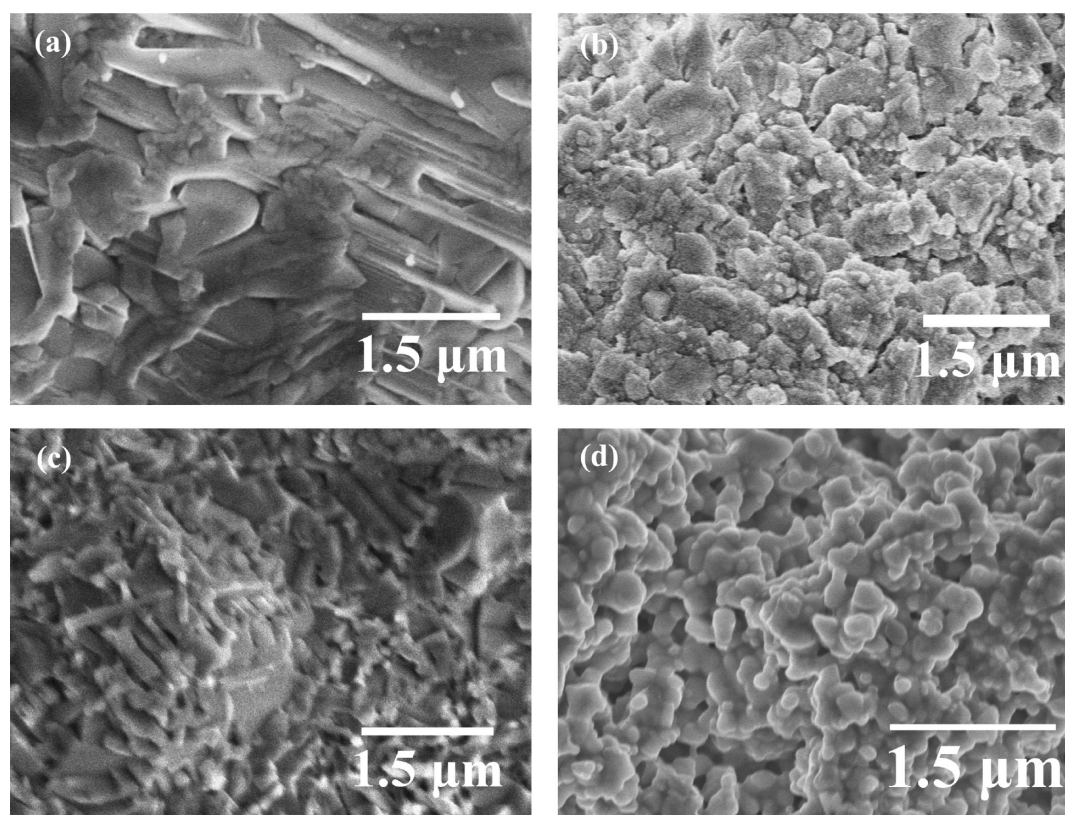

Figure 5. FESEM micrographs showing BCP/Ti nanocomposite coating before and after laser treatment. NanoHA in two different shapes were used: fiber and spherical. Dip-coated double-layer nanoHA/Ti coating, before laser treatment, (a) fiber-shaped and (b) spherical-shaped nanoHA were used. After laser coating, (c) fiber-shaped and (d) spherical-shape BCP/Ti nanocomposite were shown. Laser power used was 30 W, laser beam radius was 0.5 mm, scanning speed was 1 mm/s, and coating thickness is 40 μm. During the laser coating process, PVA was vaporized and left the coating.

3.4. Interfacial Strength between Coating and Substrate.

The interfacial bonding strength between coating and substrate was determined by scratch testing, which involves creating a controlled scratch by an indenter on the sample surface, and then analyzing the scratch via an integrated, real-time optical microscope. Observations from real-time images of the scratch are used to determine the point at which failure occurs over the progression of the scratch.

Three types of samples were evaluated: (a) Monolayer BCP/Ti nanocomposite (starting material were 50%HA/50%Ti, 20 μm thick); (b) double-layer BCP/Ti nanocomposite (starting material were 50%HA/50%Ti in the inner layer and 80%HA/20%Ti in the outer layer, 20 μm thick for each layer); (c) commercial plasma sprayed HA coating. A 50 μm diamond Rockwell indenter was drawn across the surface under incremental load from 0.1 N to 20 N with loading rate of 19.9 N/min. During loading, real-time values of friction coefficient, frictional force, normal force, acoustic emission, penetration depth, and residual depth were collected and then plotted (Figure 7). The material will start to fail at a certain critical load, marked as LC1. The critical load data are used to quantify the abrasion-resistance of the adhesive properties of different film-substrate combinations. A higher critical load usually means a larger interfacial bonding strength between layer and substrate.
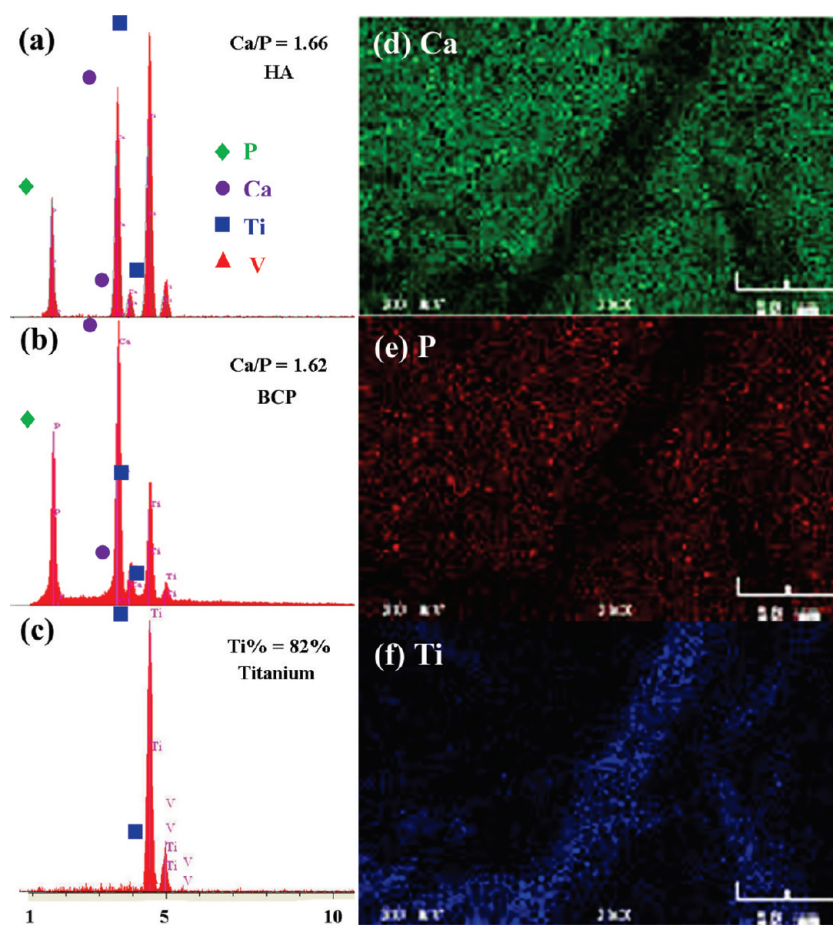
Figure 6. Typical SAEDS spectra of (a) nanoHA particles with Ca/P molar ratio of 1.66, (b) BCP composites with Ca/P molar ratio of 1.62, and (c) titanium nanoparticles, and the elemental mapping images showing (d) calcium, (e) phosphate, and (f) titanium over the same region. Double-layer laser coated sample with 40 μm thickness was used. Laser power used was 30 W, laser beam radius was 0.5 mm with scanning speed of 1 mm/s. Note: The scale bar is 20 micrometers.

The statistical data were obtained over four different scratches at each sample (Table 1). The interfacial strength of laser coated monolayer sample was comparable with that of plasma sprayed sample; and the interfacial strength of laser coated double-layer sample was more than twice of that of plasma sprayed sample. This is because the gradient multilayer nanoHA/Ti coatings alleviate the mismatch of mechanical property due to the sharp HA/substrate interface in monolayer and plasma sprayed HA coatings. The nanoBCP are entrapped firmly by molten and resolidified titanium. The BCP/Ti nanocomposite is bonded with the substrate coherently because titanium and Ti-6Al-4 V have similar thermal and mechanical properties. This strong bonding between coating layer and metal substrate makes implants suitable for load-bearing and long life cycle applications.

3.5. Qualitative Cell Culture Study. Preliminary cell culture study was performed on the BCP/Ti nanocomposite coated samples using UMR-106 osteoblast-like cells. The study was designed to qualitatively evaluate the ability of the laser coated BCP/Ti nanocomposite samples to support the adhesion and proliferation of osteoblast-like UMR-106 cells. Thus, the samples were plated with UMR-106 cells at a concentration of 200,000 cells/well in a 12-well plate. Briefly, both blank Ti-6Al-4 V substrate (control experiment) and 3 types of laser coated samples were cleaned and sterilized by immersing in absolute ethanol overnight and then washing 3 times with autoclaved Milli-Q water before

plating with cells. Two milliliters culture media (90% DMEM, 10% Fetal Bovine Serum) suspending UMR-106 cells at a concentration of 100 000 cells/mL was added to each well to completely submerge the samples. The cells were allowed to adhere and proliferate on the surfaces for 48 h before fixing and staining with crystal violet for visualization using the reported protocol.[27] Initially, we attempted to visualize the fixed and stained cells using an upright microscope with a monochrome camera. However, because of the roughness of the sample, the quality of the images was poor. This problem was solved using an Olympus SZ61 Zoom Stereo microscope. Representative stereomicroscopy images are presented in Figure 8 showing the uniform adhesion of violet-stained cells on the pure titanium, monolayer and multilayer BCP/Ti nanocomposite coated samples. To quantify cell attachment and growth on the samples, we performed the trypan blue exclusion test.[28] Briefly, UMR-106 cells proliferating on the surfaces were treated with trypsin to dislodge the cells, centrifuged, and resuspended in culture media. Trypan blue dye was added to an aliquot of the cell suspension to distinguish between dead cells (stained blue) and live cells (unstained) that were quantified with a hemocytometer.

4. DISCUSSION

4.1. Low-Power Coating Due to Increased Laser−NanoTi Interaction. Because of the strong laser-nanoTi interactions,

(a) Monolayer BCP/Ti Nanocomposite
($t = 20$ μm, $P = 18$ W, $v = 1$ mm/s, $r = 1$ mm)

(b) Double-layer BCP/Ti Nanocomposite
(($t = 40$ μm, $P = 30$ W, $v = 1$ mm/s, $r = 1$ mm)

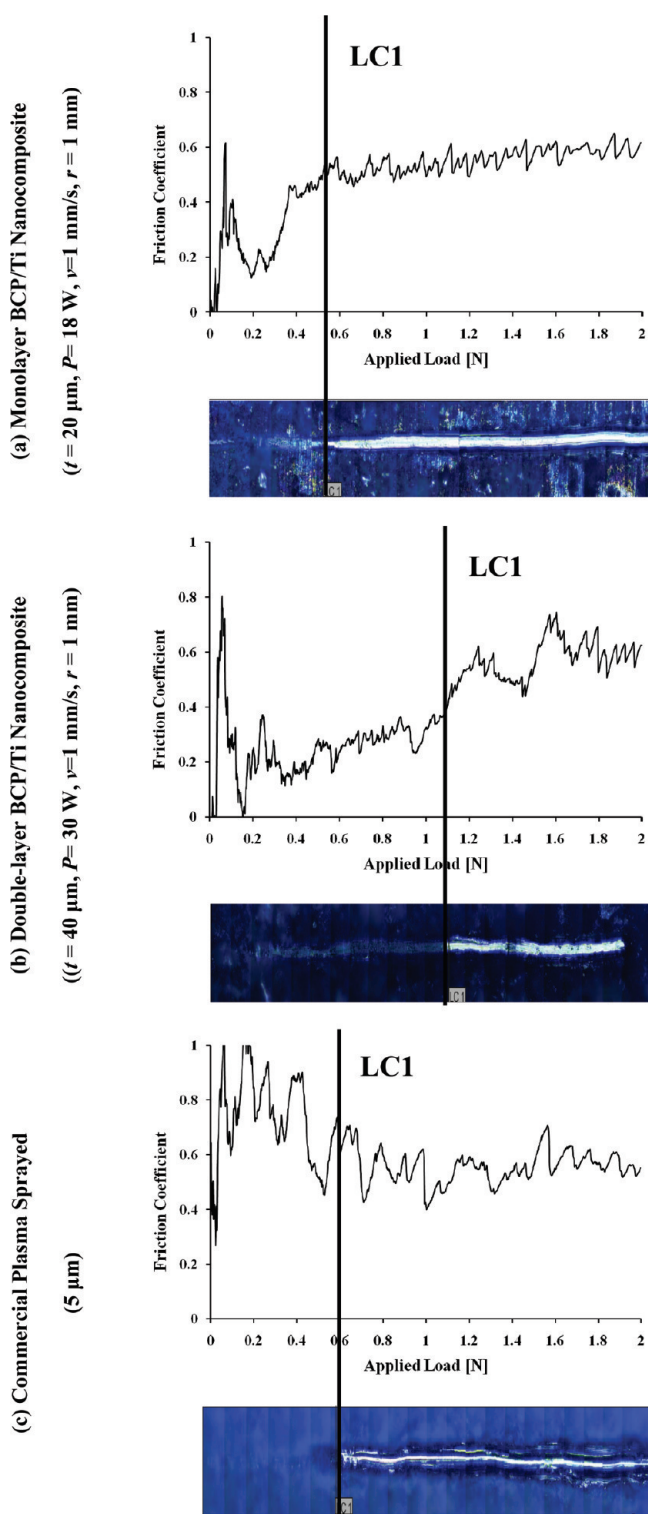**(c) Commercial Plasma Sprayed**
(5 μm)

Figure 7. Scratch testing results of three samples. The left column shows the sample number and the right column shows the resulted scratch tracks after a progressive load scratch from 0.1 N up to 20 N in one minute. Sample 1 is a mono-layer BCP/Ti nanocomposite sample with 50% HA/50% Ti as starting material; sample 2 is a double layer BCP/Ti nanocomposite sample (inner layer: 50%HA/50%Ti, outer layer: 80% HA/20%Ti as starting). Solid lines (LC1) denote the start of failing of materials, or critical load. Laser powers used were 18 and 30 W for samples 1 and 2, respectively; the laser beam radius was 0.5 mm with a scanning speed of 1 mm/s.

laser coating utilizing lower laser power is realized. When particles sizes are in the scale of nanometers, they show different properties from bulk counterparts, such as increase in plasmon resonance[29] and reduction on melting point.[30] Intrinsic properties of nanoparticles are strongly dependent on particle sizes. These unstable size-dependent properties are mainly due to higher surface atom to total atom ratio, higher surface area-to-volume ratio, and larger surface energy (surface tension) of nanoparticles.[31] When nanoparticle size is in the range of 80 nm, reduction on melting point is limited but the laser-nanoparticle interaction remains strong.[22] Strong laser-nanoparticle interaction enhances the resistive heating inside the nanoTi generating a temperature increase. Multiphysics simulation (Figure 9) shows smaller nanoTi achieves a higher temperature than larger particles at a given laser power. For instance, when laser power is 20 W, peak temperature of 1050 K is obtained for 100 nm particles; but only 380 K was obtained for 800 nm particles under the same laser power. In other words, smaller nanoparticles effectively decrease the laser power level required to perform laser coating of nanoBCP/Ti layer.

High-resolution FESEM micrographs provided stronger evidence to the surface melting and re-solidification of nanoTi during laser coating process. Figure 10 show double-layer laser coated samples before (a, b) and after (c, d) laser coating process with laser power of 30 W, laser beam radius of 0.5 mm, with a scanning speed of 1 mm/s. Before laser coating, all nanoTi appeared in the shape of spheres; however, after laser irradiation, surface melting and some complete body melting were observed under high-resolution FESEMs. Surrounding nanoTi particles were melted and merged together to form a liquid network. This network entraps nanoBCP and forms a tightly integrated BCP/Ti nanocomposite. According to calculations and temperature measurement, laser power of 30 W could generated a peak temperature of ~1160 K at the surface of the 40 μm thick BCP/Ti nanocomposite coating, while near the surface region, the temperature is close to 1660 K. Note that the IR beam of the IR camera cannot penetrate into the interfacial region to detect the temperature, thus no verification could be provided for the temperature at the coating–substrate interface. The measured temperature of 1660 K is about 262 K (13.6%) less than the calculated melting point (1922 K)[22] of 80 nm nanoTi particles. Considering the uncertainties of the temperatures measured by the IR camera, and the simplification and assumption were made to EM-HT model, the 13.6% discrepancy was acceptable. Nevertheless, more future work will be carried out to further improve the multiphysics model.

4.2. BCP/Ti Nanocomposite Enhances Biocompatibility. Both SAEDS and XRD results suggested that nanoHA was partially decomposed into β-TCP. The following reaction is believed to be responsible for this transformation[25]

$$Ca_{10}(PO_4)_6(OH)_2 (HA)$$
$$\rightarrow 2Ca_3(PO_4)_2 (TCP) + Ca_4P_2O_9 + H_2O$$
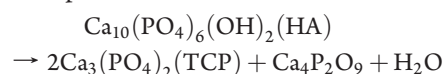
According to the Ca/P molar ratio 1.62±0.1, it can be calculated that 28% of HA has converted into β-TCP phase[32,33] with 72% of HA still exists in the BCP (with possible variation of 6%). BCP is now widely-used in many different applications due to its hybrid properties of both HA (relatively stable phase) and β-TCP (relatively unstable phase), which provides a better basis for new bone formation, delivering drugs, antibiotics, hormones,[2] and nasal septum repair.[3] Therefore, our laser coating process is also beneficial for bone formation because of the generation of BCP. In addition, absolute temperature and duration of high temperature are two important factors to induce thermal decomposition

346

dx.doi.org/10.1021/am100962m |*ACS Appl. Mater. Interfaces* 2011, 3, 339–350

Table 1. Scratch Testing Results Summary

sample number (coating thickness)		1 (20 μm)	2 (40 μm)	3 (5 μm)
	scratch 1	4.690	10.935	5.741
	scratch 2	5.575	11.173	6.349
critical load LC1, [N]	scratch 3	4.069	13.205	5.805
	scratch 4	4.519	12.549	6.060
	mean	4.713	11.966	5.989
	std. dev.	0.631	1.860	0.277

Note: Four scratch testing were conducted to each sample, then the mean of critical load values were averaged out. Sample 1 is monolayer laser coated BCP/Ti nanocomposite sample; sample 2 is multilayer laser coated sample; sample 3 is plasma sprayed sample. Both samples 1 and 2 were processed using laser beam with radius of 0.5 mm, and scanning speed of 1 mm/s. Laser power used was 18 and 30 W for samples 1 and 2, respectively.
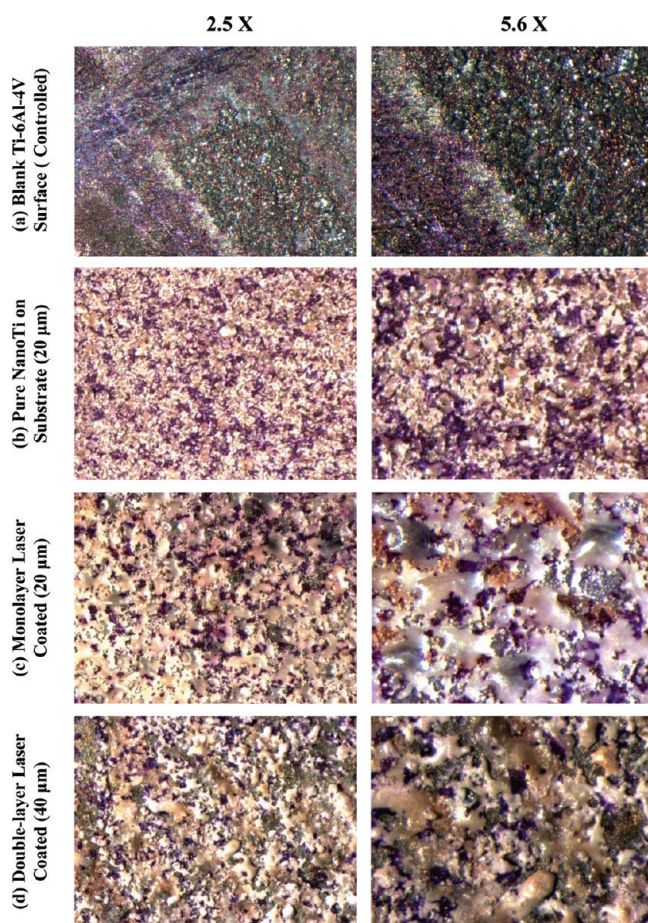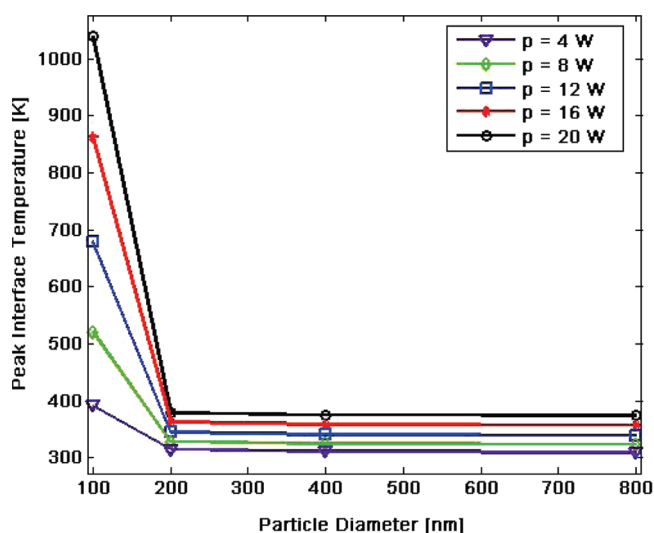

Figure 9. Multiphysics simulation calculated resulting temperature at interface region of different nanoTi particles. Resulting peak interface temperature decreases with increase of particle diameter, and size effect is more significant in small particles (<100 nm for instance). Coating layer thickness is 20 μm, laser beam radius is 0.5 mm with laser scanning speed of 1 mm/s.

Figure 8. Cell culture study with UMR-106 osteoblast cells on nano-HA/Ti coated samples. Images were taken by a stereomicroscope. (a) Blank Ti-6Al-4 V substrate with no coatings as a control experiment sample; (b) single-layer laser coating pure nanoTi coating with no nanoHA; (c) mono-layer laser coated sample with 50% HA/50% Ti; (d) double-layer laser coated sample (inner layer: 50%HA/50%Ti, outer layer: 80%HA/20%Ti).

of HA. By controlling the laser power and irradiation time, it is possible to manipulate the conversion rate of HA to β-TCP, which would be potentially an ideal method to create BCP with different Ca/P molar ratios. This is one of the advantages of the laser coating technique.

Some recent studies revealed that nanoscale bioceramics have the following improved biocompatibilities over microscale or larger counterparts. First, nanoscale biomaterial attracts a greater number of osteoblasts, i.e., bone-producing cells, and increase the activity of bone cells on the surface of implants.[34,35] Consequently, they improve the strength between implants and natural bone host. More extensive bone formation also occurs in samples with nanoscale features as compared to electropolished implants.[36] Likewise, nanoHA has been shown to support the attachment and growth of human osteoblast-like cells while preventing significant inflammatory responses.[37] Second, nanoscale biomaterial has higher surface area, thus enhancing the osteoblast adhesion.[38-40] Third, the biodegradation of nanoscale biomaterials is much faster[41] than micrometer scale materials. Nanoscale biomaterial is also easier to be remodeled and integrated to bone by osteoblasts, which greatly reduces the infection and pain.[42]

The preliminary results of the cell culture experiment showed more cell growth on both single and multilayer BCP/Ti nanocomposite compared with blank Ti-6Al-4 V substrate (Sample (a) of Figure 8) and pure nanoTi coated sample (sample b in Figure 8). Using the trypan blue exclusion test, the UMR-106 cells proliferating on the surfaces were detached by treatment with trypsin, and quantified with a hemocytometer after staining with trypan blue. The result showed that after culturing cells for 4 days, the cell proliferating were barely observed on blank Ti-6Al-4 V substrate, and the cells proliferating on both the single and multilayer BCP/Ti nanocomposite were two times greater (~20 vs. 10 cells/μL) than those on pure titanium-coated samples. The existence of BCP/Ti nanocomposites are responsible for the better biocompatibility for both single and double BCP/Ti coated samples. And TiO$_2$ (due to oxidization of Ti nanoparticles during laser coating process) on pure nanoTi substrate is believed to be responsible for biocompatibility which is worse than BCP/Ti coated samples, but better than blank Ti-6-Al-4 V substrate. A
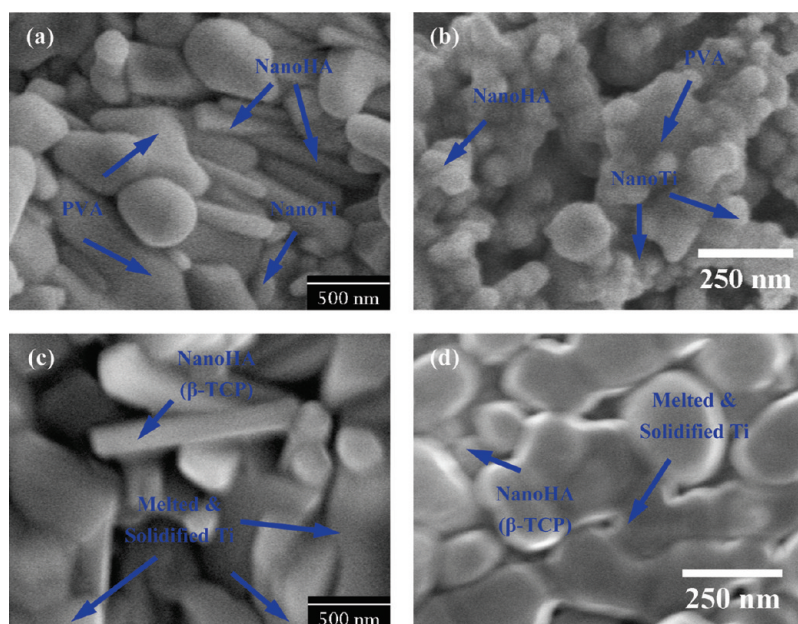
347

dx.doi.org/10.1021/am100962m |ACS Appl. Mater. Interfaces 2011, 3, 339–350

Figure 10. Laser coated BCP/Ti nanocomposite sample was characterized via FESEM. Before laser coating: dip-coated nanoHA/nanoTi layer, (a) fiber-shaped and (b) spherical-shaped nanoHA. After laser coating: (c) fiber-shaped and (d) spherical nanoHA/β-TCP + Ti. Melting of nanoTi was observed after laser coating. The physical appearance of some nanoHA was maintained after laser treatment. PVA was thermally desorbed from the coating layer. Laser power used was 30 W, laser beam radius was 0.5 mm with scanning speed of 1 mm/s.
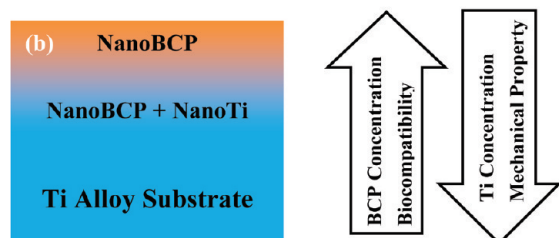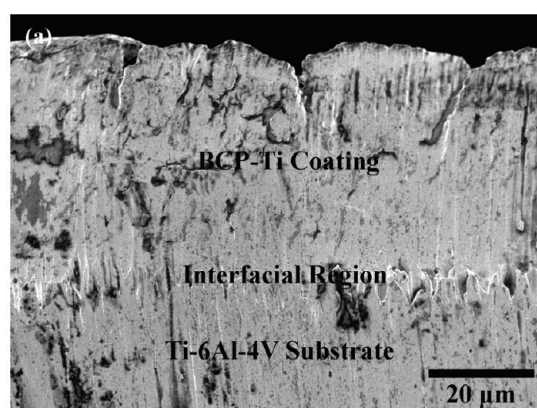

Figure 11. (a) Cross-section FESEM images of laser coated double-layer BCP/Ti nanocomposite. (b) Schematic of nanoBCP coating/substrate interface of functional gradient coating. Functional gradient coating has smooth transition in material properties, such as mechanical property, and biocompatibility. A solid interfacial bonding can also be achieved via laser coating technique.

comprehensive study to quantify the gene expression of bone-related characteristics on UMR-106 cells grown on these samples will be conducted and reported in due course.

4.3. Functional Gradient Coating Improves the Interfacial Strength between Coating and Substrate. Novel microstructure

with functional gradient coating was obtained. Cross-section FESEM images of laser coated BCP/Ti nanocomposite were taken, as shown in Figure 11a. FESEM images show the thickness of each layer was about 20 μm, in good agreement with the micrometer measurement and the thickness used in multiphysics simulation. It also shows good homogeneity of laser coating BCP/Ti nanocomposite film, with a solid interfacial bonding between coating and substrate. The substrate has a zigzag morphology, which was introduced during the substrate sand-paper polishing procedure. Laser coating is a non-equilibrium process involving fast heating process (in the scale of microsecond), which produces metastable phases by exceeding the solid-solubility limit beyond the equilibrium phase diagram. This could lead to fine titanium grain structure. NanoBCP and nanoTi form a composite coating structure. With gradual variation in the ratio of nanoBCP and nanoTi, as shown in Figure 11b, coating/substrate interfacial bonding strength was determined to be superior to the commercial plasma spraying method. Strong coating/substrate interfacial bonding is obtained because the replaced ceramic composite precursor is entrapped with a thin layer of the molten titanium to produce a laser-melt zone; these coatings are metallurgically bonded, providing a sound and adherent interface between the coating and substrate. In Figure 11a, BCP has a high concentration near the surface, whereas nanoTi has higher concentration near the coating/substrate interface. The high concentration of nanoTi in the coating/substrate interface minimizes the mismatch of thermal and mechanical properties since nanoTi has similar properties as the Ti-6Al-4 V substrate.[17] Moreover, it is expected that the fine phases formed at the bioceramics/metal interface due to high cooling rate can further reduce the chances of crack propagation.[43]

5. CONCLUSIONS

Multilayer laser coating of BCP/Ti nanocomposite on metal substrates is presented. We have demonstrated a coating process for multilayer of BCP/Ti nanocomposite on Ti-6Al-4 V

substrates. This unique gradient coating structure has very good mechanical property, and also promotes cell attachment and proliferation. The coated samples are characterized using FES-EM, SAEDS, elemental mapping, XRD, and scratch testing. Preliminary in vitro study shows the preferential growth of osteoblast-like UMR-105 cells on the BCP/Ti nanocomposite surfaces. The following three objectives have been also achieved.

(1) Low laser power processing is realized. Because of the size effect on nanoparticles, significant increase in laser—particle interactions is expected from nanoTi used. The presence of titanium nanoparticles also provides a stronger interfacial strength compared with plasma sprayed technique.

(2) BCP/Ti nanocomposite coating with good mechanical properties (high surface hardness, and strong interfacial strength between coating and substrate), beneficial microstructure, and biocompatible phases (nanoHA and β-TCP) are obtained using laser coating technique. The formation and adhesion of BCP to metal substrate is realized at the same time.

(3) Multiphysics model to describe the laser-nanoparticle interaction and heat transfer within nanoparticles is established, and validated with experiments. Optimal processing conditions for experiments are found under the guidance of simulation results.

For an ideal functional gradient multilayer coating, nanoHA/Ti mixture with variable nanoHA concentration from 100% at the top to 0% on the interface could be used. The scheme that has pure nanoBCP at top surface and pure nanoTi on the interface would avoid sharp change in material properties while interfacial bonding strength and top surface biocompatibility are well maintained.

■ ASSOCIATED CONTENT

Ⓢ **Supporting Information.**   More details about the multiphysics finite element method simulation could be found in supporting information. It includes: (i) how the multiphysics model is built; (ii) what is the electromagnetic module and heat transfer module; (iii) how the electromagnetic and heat transfer modules are coupled; and (iv) typical resulting resistive heating and temperature carried out by the multiphysics simulation. This material is available free of charge via the Internet at http://pubs.acs.org/.

■ AUTHOR INFORMATION

Corresponding Author
*E-mail: gjcheng@purdue.edu.

■ ACKNOWLEDGMENT

■ ABBREVIATIONS USED

BCP	biphasic calcium phosphate
CW	continuous wave
EDS	energy-dispersive X-ray spectrometry
EM	electromagnetic
FESEM	field-emission scanning electron microscopy
HA	hydroxyapatite
HT	heat transfer
IR	infrared
LC1	critical load
nanoHA	HA nanoparticles
nanoTi	Ti nanoparticles
nanoHA/Ti	nanoHA and nanoTi mixture
Nd:YAG	neodymium-doped yttrium aluminium garnet
PDF	Powder Diffraction File
PVA	polyvinyl alcohol
ROI	region of interest
SAEDS	selected area energy-dispersive X-ray spectrometry
TCP	tricalcium phosphate
Ti	titanium
XRD	X-ray diffraction
β-TCP	beta-tricalcium phosphate

■ REFERENCES

(1) Zhu, Z. L.; Yu, H. Y.; Zen, Q.; He, H. W. *Appl. Surf. Sci.* **2008**, *255*, 552–554.

(2) Kamatakahara, M.; Ohtsuki, C.; Miyazaki, T. *J. Biomater. Appl.* **2008**, *23*, 197–212.

(3) Gabory, L.; Bareille, R.; Stoll, D.; Bordenave, L.; Fricain, J. C. *Acta Biomater.* **2010**, *6*, 909–919.

(4) Legeros, R. Z. *Adv. Dent. Res.* **1988**, *2*, 165–180.

(5) Daculsi, G. *Biomaterials* **1998**, *19*, 1473–1478.

(6) Ramay, H.; Zhang, M. *Biomaterials* **2004**, *25*, 5171–5180.

(7) Goyenvaalle, E.; Guyen, N. J. M.; Aguado, E.; Passuti, N.; Daculsi, G. *J. Mater. Sci. Mater. Med.* **2003**, *14*, 219–227.

(8) Redepenning, J.; Schlessinger, T.; Burnham, S.; Lippiello, L.; Miyano, J. *J. Biomed. Mater. Res.* **1996**, *30*, 287–294.

(9) Babu, N. R.; Manwalkar, S.; Rao, K. P.; Kumar, T. S. *Trends Biomater. Artif. Organs* **2004**, *17*, 43–47.

(10) Kim, H. W.; Kim, H. E.; Knowles, J. C. *Key Eng. Mater.* **2004**, *254-256*, 1103–1106.

(11) LeGeros, J. P.; Lin, S.; Mijare, D.; Dimaano, F.; LeGeros, R. Z. *Key Eng. Mater.* **2005**, *284-286*, 247–250.

(12) Zhang, L.F.; Sun, R.; Xu, L.; Du, J.; Xiong, Z. C.; Chen, H. C.; Xiong, C. D. *Mater. Sci. Eng., C* **2008**, *28*, 141–149.

(13) Benhayoune, H.; Drevet, R.; Faure, J.; Potiron, S.; Gloriant, T.; Oudadesse, H.; Laurent-Maquin, D. *Adv. Eng. Mater.* **2010**, *12*, B192–199.

(14) Cho, J. S.; Ko, Y.N.; Koo, H.Y.; Kang, Y.C. *J. Mater. Sci. Mater. Med.* **2010**, *21*, 1143–1149.

(15) Comesaña, R.; Quintero, F.; Lusquiños, F.; Pascual, M. J.; Boutinguiza, M.; Durán, A.; Pou, J. *Acta Biomater.* **2010**, *2*, 953–961.

(16) Brossa, F.; Cigada, A.; Chiesa, R.; Paracchini, L.; Consonni, C. *Biomed. Mater. Eng.* **1993**, *3*, 127–136.

(17) Cheng, G.J.; Pirzada, D.; Cai, M.; Mohanty, P.; Bandyopadhyay, A. *Mater. Sci. Eng., C* **2005**, *25*, 541–547.

(18) Nanda, K. K.; Maisels, A.; Kruis, F. E.; Fissan, H.; Stappert, S. *Phys. Rev. Lett.* **2003**, *91*, 106102.

(19) Hao, E.; Schatz, G. C. *J. Chem. Phys.* **2004**, *120*, 357–366.

(20) Tsui, Y. C.; Doyle, C.; Clyne, T. W. *Biomaterials* **1998**, *19*, 2015–2029.

(21) Balasundaram, G.; Sato, M.; Webster, T. *Biomaterials* **2006**, *27*, 2798–2805.

(22) Zhang, M.Y.; Cheng, G.J. *J. Appl. Phys.* **2010** in press.

(23) Stratton, J. A. *Electromagnetic Theory*; McGraw-Hill: New York, 1941.

(24) Qiu, T. Q.; Tien, C. L. *Int. J. Heat Mass Tran.* **1992**, *35*, 719–725.

(25) Locardi, B.; Pazzaglia, U. E.; Gabbi, C.; Profilo, B. *Biomaterials* **1993**, *14*, 437–441.

(26) Strawhecker, K. E.; Manias, E. *Chem. Mater.* **2000**, *12*, 2943–2949.

(27) Freshney, I. *Culture of Animal Cells*, 5th ed.; John Wiley & Sons: New York, 2005; pp 252−253.

(28) Freshney, I. *Culture of Animal Cells*, 5th ed.; John Wiley & Sons: New York, 2005; p 361.

(29) Kelly, K. L.; Coronado, E.; Zhao, L. L.; Schatz, G. C. *J. Phys. Chem. B* **2003,** *107*, 668–677.

(30) Safaei, A.; Shandiz, M. A.; Sanjabi, S.; Barber, Z. *J. Phys. Chem. C* **2008,** *112*, 99–105.

(31) Nanda, K. K.; Maisels, A.; Kruis, F. E. *J. Phys. Chem. C* **2008,** *112*, 13488–13491.

(32) Locardi, B.; Pazzaglia, U. E.; Gabbi, C.; Profilo, B. *Biomaterials* **1993,** *14*, 437–441.

(33) Balamnrugan, A.; Rebelo, A. H. S.; Kannan, S.; Ferreira, J. M. F.; Michel, J.; Balossier, G.; Rajeswari, S. *J. Biomed. Mater. Res., B: Appl. Biomater.* **2007,** *81B*, 441–447.

(34) Kannan, S.; Rocha, J. H. G.; Ventura, J. M. G.; Lemos, A. F.; Ferreira, J. M. F. *Scr. Mater.* **2005,** *53*, 1259–1262.

(35) Huang, J.; Lin, Y. W.; F X., W.; Best, S. M.; Brooks, R. A.; Rushton, N.; Bonfield, W. *J. Mater. Sci. Mater. Med.* **2007,** *18*, 2151–2157.

(36) Price, R. L.; Gutwein, L. G.; Kaledin, L.; Tepper, F.; Webster, T. J. *J. Biomed. Mater. Res., A* **2003,** *15*, 1284–1293.

(37) Meirelles, L.; Arvidsson, A.; Andersson, M.; Kjellin, P.; Albrektsson, T.; Wennerberg, A. *J. Biomed. Mater. Res.* **2008,** *87A*, 229–307.

(38) Huang, J.; Best, S. M.; Bonfield, W.; Brooks, R. A.; Rushton, N.; Jayasinghe, S. N.; Edirisinghe, M. J. *J. Mater. Sci.—Mater.* **2004,** *15*, 441–445.

(39) Boissard, C. I. R.; Bourban, P. E.; Tami, A. E.; Alini, M.; Eglin, D. *Acta Biomater.* **2009,** *5*, 3316–3327.

(40) Webster, T. J.; Siegel, R. W.; Bizios, R. *Biomaterials* **1999,** *20*, 1221–1227.

(41) Price, R. L.; Ellison, K.; Haberstroh, K. M.; Webster, T. J. *J. Biomed. Mater. Res A* **2004,** *70A*, 129–138.

(42) Streicher, R. M.; Schmidt, M.; Fiorito, S. *Nanomedicine* **2007,** *2*, 861–874.

(43) Jain, K. K.; *The Handbook of Nanomedicine*; Humana Press: Totowa, NJ, 2008; Chapter 10: Nano-Orthopedics.